International Journal of Heat and Fluid Flow 30 (2009) 1142–1156

Contents lists available at ScienceDirect

International Journal of Heat and Fluid Flow

journal homepage: www.elsevier.com/locate/ijhff

Two-way coupled simulation of a flow laden with metallic particulates in overexpanded TIC nozzle

Abouzar Moshfegh [a], Mehrzad Shams [a,*], Reza Ebrahimi [b], Mohammad Ali Farnia [b]

[a] Faculty of Mech. Engng., K.N. Toosi University of Tech., Pardis St., Vanak Sq., Tehran 19395-1999, Iran
[b] Faculty of Aerospace Engng., K.N. Toosi University of Tech., East Vafadar St., Tehranpars Ave., Tehran 16765-3381, Iran

ARTICLE INFO

Article history:
Received 25 September 2008
Received in revised form 15 July 2009
Accepted 3 September 2009
Available online 9 October 2009

Keywords:
Gas–solid flow
TIC nozzle
CFD
Two-way coupling
Separation point transition

ABSTRACT

A simulation of non-reacting dilute gas–solid flow in a truncated ideal contour nozzle with consideration of external stream interactions is performed. The Eulerian–Lagrangian approach involving a two-way momentum and thermal coupling between gas and particles phases is also adopted. Of interests are to investigate the effects of particles diameter and mass flow fraction on the flow pattern, Mach number, pressure and temperature contours and their distributions along the nozzle centerline and wall. The main goal is to determine the separation point quantitatively when the particles characteristics change. Particles sample trajectories are illustrated throughout the flow field and a qualitative discussion on the way that physical properties of the nozzle exit flow and particles trajectories oscillate is prepared. The existence of solid particulates delays the separation prominently in the cases studied. The bigger particles and the higher particles mass flow fractions respectively advance and delay the separation occurrence. The particles trajectories oscillate when they expose to the crisscrossing (or diamond-shape) shock waves generated outside the nozzle to approach the exit jet conditions to the ambient. The simulation code is validated and verified, respectively, against a one-phase 2D convergent–divergent nozzle flow and a two-phase Jet Propulsion Laboratory nozzle flow, and acceptable agreements are achieved.

1. Introduction

The existence of metallic fuel constituents in modern solid-propellants has brought so much attention to the gas–solid two-phase flows in nozzles. Solid metal oxide combustion products deteriorate the expansion quality of nozzles in converting the thermal combustive energy to the kinetic one. The velocity and thermal slippage between micron-sized solid particles and gaseous carrier phase, whereby the momentum and energy are transferred between two phases, can be accounted as the major reason to the loss of nozzle performance. Experiments show that the magnitude of such losses increases with the weight fraction of particles (Hoglund, 1962). It is necessary to know the behavior of the two-phase flow expanding through the nozzle in order to evaluate the motor performance. Meanwhile, a successful prediction of the thermo-fluid mechanical characteristics development of gas and particles is very crucial and imperative for the successful design and operation of rocket nozzles and energy conversion systems.

Pioneering investigations on the particle-laden nozzle compressible flows served to place bounds on the performance losses by examining the limiting cases of no-slippage and complete slippage. Gilbert et al. (1955) simulated the gas–solid flow by implementing of Stokes' law to account for the drag force acting on particles for the case of linearly accelerated nozzle gas. They demonstrated that 1 μm particles follow approximately the gas streamlines, whereas the 10 μm particles have a significant lag in receiving the momentum and thermal energy from the carrier phase. Altman and Carter (1956) reported that velocity slippage has a more effect on the specific impulse than does the thermal slippage. The first coupled gas–solid two-phase flow solution was analytically given by Carrier (1958). The solution dealt with interactions between particles and normal shock wave. He found that both inviscid gas and particle velocity decrease across the normal shock, while the gas pressure and density rise correspondingly. He also reported that the relaxation process is dominated by the momentum interchange not the thermal exchange. Kliegel (1959) did a similar one-dimensional inviscid analysis in the nozzle considering instantaneous velocity and thermal slippage and the reciprocal effects of particles on gas medium. Lype's (1605) proposed the equations including viscous dissipation in the gas, heat transfer losses, and buoyancy forces on the particles. Since the 1970s, numerical methods have been broadly applied to a complicated set of governing equations. Chang (1980) used the MacCormack scheme to study the unsteady gas–particle equations in

* Corresponding author.
E-mail address: shams@kntu.ac.ir (M. Shams).

0142-727X/$ - see front matter Crown Copyright © 2009 Published by Elsevier Inc. All rights reserved.
doi:10.1016/j.ijheatfluidflow.2009.09.001

Nomenclature

x, y	Cartesian coordinates (m)
k	conductivity coefficient (N/s K)
F, **G**	convective flux vectors (kg/m^2 s)
S_{ph}	energy source term (kg m/s^2)
h	enthalpy per unit mass (m^2/s^2)
R	gas constant (J/kg K)
q_x, q_y	gas heat flux components (N/m s)
Pr	gas Prandtl number
P	gas pressure (N/m^2)
C_p	gas specific heat at constant pressure (J/kg K)
E	gas specific total energy per unit mass (m^2/s^2)
x_t	horizontal location of nozzle throat (m)
J	Jacobian
T_∞	local bulk temperature of the gas surrounding the particle (K)
M	Mach number
S	molecular speed ratio
A	nozzle cross section area (m^2)
NTP	number of trajectories of particles
hc	particle convective heat transfer coefficient (W/m^2 K)
d_P	particle diameter (μm)
m_P	particle mass (kg)
Nu_P	particle Nusselt number
Re	particle relative Reynolds number
C	particle specific heat (J/kg K)
C_D	particle total drag coefficient
V	particle vector of velocity (m/s)
A_P	projected area of spherical particle (m^2)
$\dot{Q}$	pure rate of heat transfer to/from the particle (W)
T	temperature (K)
t	time (s)
S	two-way coupling source terms (kg/m^2 s)
Q	vector of conservative flow dependent variables (kg/m^2 s)
U	vector of gas velocity (m/s)
u, v	velocity components (m/s)
$\mathbf{F}_v$, $\mathbf{G}_v$	viscous flux vectors (kg/m^2 s)
S_{pu}	x-momentum source term (kg m/s^2)
S_{pv}	y-momentum source term (kg m/s^2)

Greek symbols

ρ_{ambient}	ambient flow density (kg/m^3)
λ	coefficient of bulk viscosity (N s/m^2)
ρ_{jet}	exit jet density (kg/m^3)
ρ	gas density (kg/m^3)
μ	gas dynamic viscosity (N s/m^2)
ξ, η	generalized curvilinear coordinates
δ_{ij}	Kronecker delta function
γ	ratio of gas specific heats
τ_{xx}, τ_{xy}, τ_{yy}	shear stress components (N/m^2)

Superscript

^	transformed variables

Subscripts

a	ambient
x, y	Cartesian directions
c	combustion
p	constant pressure
e	exit
g	gas
i, j	indicial notation
P	particle
sep	separation
0	stagnation
t	throat
v	viscous flux vector indicator
w	wall

conservation form in axisymmetric convergent–divergent nozzles (Jet Propulsion Laboratory (JPL) nozzle, and Titan III and IUS solid rocket motors) by changing some parameters like particles diameter and mass flow fraction. Marconi et al. (1981) used the characteristic method to analyze the one-dimensional unsteady particle-laden gas flows.

A complete review of numerical models for simulation of dilute gas–particle flows was presented by Crowe (1982) who also categorized these models according to their order of coupling, and types of dimension and approach. The advantages and disadvantages of two-fluid and trajectory models were also discussed therein. A numerical study of the gas–particle flow in a solid motor nozzle was made by Hwang and Chang (1988) using the MacCormack's explicit scheme in conjunction with a trajectory model. Gokhale and Bose (1989) extended a non-reacting two-phase flow study to the reacting one in a one-dimensional nozzle using the explicit MacCormack's scheme. Nishida and Ishimaru (1990) simulated the gas–solid two-phase non-equilibrium nozzle flows using MacCormack's scheme with total variation diminishing (TVD) method. Mehta and Jayachandran's work (1998) developed a fast numerical algorithm to simulate the two-phase viscous flows in axisymmetric convergent–divergent nozzles. An Eulerian–Eulerian approach with appropriate exchange terms for gas–particle interaction was used to simulate the coupled gas–particle flow in a Jet Propulsion Laboratory (JPR) nozzle. Igra et al. (1999) investigated two-phase flow in the nozzle outside free stream as well as the nozzle inside flow. Bendor et al. (2001) studied various reflection patterns of planar shock waves from straight wedges in dust-gas suspensions. The results provided a clear picture of whether and how the presence of dust particles affects the shock-reflection-induced flow field. A quasi-1D model was performed to consider the non-equilibrium effects of the gas phase with high reduced temperature in a particle-laden conical nozzle for coating applications (Luo et al., 2008). Apart from the chemical rate equations, the atomic species concentration equations were also solved. This model is used for the design and optimization of the nozzle geometry by a parametric study.

In the present study, an Eulerian–Lagrangian approach involving a two-way momentum and thermal coupling between gas and particles exchanges is adopted to simulate the non-reacting dilute gas–solid axisymmetric flow in a truncated ideal contour (TIC) nozzle with consideration of external stream interactions. The combustion products are assumed to be included by aluminium oxide particulates that play the role of solid dispersed phase in this flow case study. Of interests are to investigate the effects of particles on the flow pattern, Mach number, pressure and temperature contours and their distributions along the nozzle centerline and wall. The main goal is to determine the separation point quantitatively and its variations versus the particles diameter and mass flow fraction. A same study was presented previously by Moshfegh et al. (1081) to investigate the separation point transition in a one-phase TIC nozzle flow. Particles sample trajectories are illustrated

throughout the flow field, and a qualitative discussion on the way that the external compressible flow properties and particles trajectory oscillate is prepared. The simulation code is validated and verified respectively against a one-phase 2D-CD nozzle flow and a two-phase JPR nozzle flow, and acceptable agreements are achieved.

2. Two-phase flow governing equations

2.1. Carrier phase

The Navier–Stokes governing equations for non-reacting flow are considered to be time-dependent, two-dimensional and compressible. Written in Cartesian coordinates and strong conservative form (Tsai and Hsieh, 1990), the mass, momentum and energy governing equations are expressed as follow

$$\frac{\partial \mathbf{Q}}{\partial t}+\frac{\partial}{\partial x}(\mathbf{F}-\mathbf{F}_v)+\frac{\partial}{\partial y}(\mathbf{G}-\mathbf{G}_v)=\mathbf{S} \tag{1}$$

where $\mathbf{Q}$ is the vector of conservative flow dependent variables, $\mathbf{F}$ and $\mathbf{G}$ are the convective flux vectors and $\mathbf{F}_v$ and $\mathbf{G}_v$ are the viscous flux vectors which all are given below. The vector $\mathbf{S}$ includes the source terms issuing from considering the dispersed phase effects on the carrier one, and will be discussed perfectly in the next Section 2.2.

$$\mathbf{Q}=\begin{bmatrix}\rho\\ \rho u_g\\ \rho v_g\\ \rho E\end{bmatrix},\quad \mathbf{F}=\begin{bmatrix}\rho u_g\\ \rho u_g^2+p\\ \rho u_g v_g\\ u_g(\rho E+p)\end{bmatrix},\quad \mathbf{G}=\begin{bmatrix}\rho v_g\\ \rho u_g v_g\\ \rho v_g^2+p\\ v_g(\rho E+p)\end{bmatrix} \tag{2}$$

$$\mathbf{F}_v=\begin{bmatrix}0\\ \tau_{xx}\\ \tau_{xy}\\ u_g\tau_{xx}+v_g\tau_{xy}-q_x\end{bmatrix},\quad \mathbf{Q}_v=\begin{bmatrix}0\\ \tau_{xy}\\ \tau_{yy}\\ u_g\tau_{xy}+v_g\tau_{yy}-q_y\end{bmatrix} \tag{3}$$

In the preceding expressions, the specific total energy (E), the shear stress components (τ) and the heat flux statement (q), are denoted by

$$E=h_g-\frac{p}{\rho}+\frac{1}{2}\left(u_g^2+v_g^2\right),$$
$$\tau_{ij}=\mu\left(\frac{\partial u_{g_i}}{\partial x_j}+\frac{\partial u_{g_j}}{\partial x_i}\right)+\delta_{ij}\lambda div\mathbf{U},\quad q_i=-k_g\frac{\partial T_g}{\partial x_i} \tag{4}$$

In these formulations, u_g and v_g are velocity components of gas in Cartesian coordinates (x, y), t is the time, ρ is the gas density, p is the gas pressure, h_g is the gas enthalpy, μ is the fluid dynamic viscosity, δ_{ij} is the Kronecker delta function, λ is the coefficient of bulk viscosity, $\mathbf{U}$ is the vector of gas velocity, k_g is the gas conductivity coefficient and T_g is the gas temperature. The gas enthalpy is obtained by an integration of specific heat at constant pressure (C_p) and varying temperature

$$h_g=\int_0^T C_p dT_g \tag{5}$$

Body forces are assumed to be negligible. The flow is considered to be a single-specie, and its thermodynamic properties are generally determined by assuming that the flow behaves as a perfect gas. The forth order temperature-dependent polynomial (Warren et al., 1988) used to calculate the gas conductivity coefficient (k_g), the gas specific heat at constant pressure (C_p) and the gas dynamic viscosity (μ), is expressed by

$$\begin{Bmatrix}k_g\\ C_p\\ \mu\end{Bmatrix}=\sum_{N=0}^{4}Z_N T_g^N \tag{6}$$

where Z_N is the coefficient of temperature at each series term that is replaced according to the (Table 1).

2.2. Dispersed phase

The flow can be considered dilute if the effects of particle–fluid interactions dominate the overall dispersion and deposition of particles. If the particle–particle interactions dominate, the flow is regarded as dense flow. The particle velocity and temperature do not immediately respond to a physical change in gas because of the inertia and heat capacity the particles have.

In this study, the particles are assumed to be solid, smooth, spherical, irrotational, impermeable, neutral electrically, non-deformable, homogenous and thermally lumped with constant physical and thermodynamical properties. There are no mass or energy losses from the system. Ounis and Ahmadi (1990) showed that other hydrodynamical forces such as the Basset history, the virtual mass, the pressure gradient and Faxen correction terms are much smaller than the drag force for small particles. The Brownian motion and Saffman's lift force are also negligibly small. The volume occupied by the particles is negligible, so the particles do not interact with each other (collisionless motion). Therefore, the gas–particle flow can be regarded as dilute. Convection is assumed to be the only way to transfer heat from gas to particles. The effect of the conduction and radiative heat transfer between two phases is neglected.

Because of the non-uniform distribution of particles within the flow field, there are some considerable areas where do not include any particle. This can be regarded as the main reason to higher accuracy of Lagrangian approach vs. the Eulerian one in the dilute regimes. Lagrangian tracking of aerosol particles depends upon their individual acting forces expressed as a function of gas–particle interfacial variables (Reynolds and Nusselt numbers, and etc.). In the present simulation, we consider the drag force through the following expression

$$m_P\frac{d\mathbf{v}}{dt}=\rho C_D(\mathbf{U}-\mathbf{v})|\mathbf{U}-\mathbf{v}|\frac{A_P}{2} \tag{7}$$

where m_P is the particle mass, $\mathbf{v}$ is the vector of particle velocity, t is the time, C_D is the coefficient of total drag force acting on the

Table 1
Constant coefficients of the Eq. (6).

	k_g (W/m K)	C_p (kJ/kg K)	μ (N s/m^2)	
			250 K $\leqslant T_g <$ 600 K	600 K $\leqslant T_g$
Z_0	$-2.276501\times10^{+1}$	0.103409×10^{-3}	-9.8601×10^{-1}	4.8856745
Z_1	1.2598485×10^{-4}	-0.2848870×10^{-3}	9.080125×10^{-2}	5.43232×10^{-2}
Z_2	-1.4815265×10^{-7}	0.7816818×10^{-6}	-1.17635575×10^{-4}	-2.4261775×10^{-5}
Z_3	1.73550646×10^{-10}	-0.4970786×10^{-9}	1.2349703×10^{-7}	7.9306×10^{-9}
Z_4	-1.066657×10^{-13}	0.1077024×10^{-12}	-5.7971299×10^{-11}	-1.10398×10^{-12}

particle, and A_P is the projected area of the spherical particle. Particle total drag coefficient in a relative compressible flow between the gas and particle was formulated by Henderson (1976) Eqs. (8) and (10) and Carlson and Hoglund (1964) Eq. (9) separately in both subsonic and supersonic relative regimes as given below

$$C_D|_{M_P<1} = 24\left\{\mathrm{Re}_P + S\left[4.33 + 1.567\times\exp\left(-0.247\frac{\mathrm{Re}_P}{S}\right)\right]\right\}^{-1} + \left[1-\exp\left(-\frac{M_P}{\mathrm{Re}_P}\right)\right]0.6S + \exp\left(-\frac{0.5M_P}{\sqrt{\mathrm{Re}_P}}\right)\left[\frac{4.5+0.38(0.03\mathrm{Re}_P+0.48\sqrt{\mathrm{Re}_P})}{1+0.03\mathrm{Re}_P+0.48\sqrt{\mathrm{Re}_P}}+0.1M_P^2+0.2M_P^8\right] \tag{8}$$

$$C_D|_{1<M_P<1.75} = \frac{24\left[1+\exp\left(-\frac{0.427}{M_P^{4.63}}-\frac{3}{\mathrm{Re}_P^{0.88}}\right)\right]}{\mathrm{Re}_P + M_P[3.82+1.28\exp(-1.25\mathrm{Re}_P/M_P)]} \tag{9}$$

$$C_D|_{M_P>1.75} = \frac{0.9+\frac{0.34}{M_P^2}+1.86\left(\frac{M_P}{\mathrm{Re}_P}\right)^{1/2}\left[2+\frac{2}{S^2}+\frac{1.058}{S}-\frac{1}{S^4}\right]}{1+1.86\left(\frac{M_P}{\mathrm{Re}_P}\right)^{1/2}} \tag{10}$$

where the Re_P is the particle relative Reynolds number, M_P is the particle relative Mach number and S is the molecular speed ratio. These variables are defined locally in the following forms

$$\begin{bmatrix}\mathrm{Re}_P\\ M_P\\ S\end{bmatrix} = |\mathbf{U}-\mathbf{v}|\begin{bmatrix}\rho d_P/\mu\\ (\gamma RT_g)^{-1/2}\\ (2RT_g)^{-1/2}\end{bmatrix} \tag{11}$$

Here, d_P is the spherical particle diameter, γ is the ratio of gas specific heats, and R is the gas constant. The thermal governing equation for the particle temperature changes is formulated by

$$m_P C\frac{dT_P}{dt} = \dot{Q} = \pi hcd_P^2(T_P - T_\infty) \tag{12}$$

where C is the specific heat of particle, T_P is the temperature of the lumped particle whose internal thermal resistance is neglected, $\dot{Q}$ is the pure rate of total heat transfer to/from the particle, hc is the coefficient of convective heat transfer, and T_∞ is the local bulk temperature of the fluid surrounding the particle. Benefiting the definition of Nusselt number, the Eq. (12) can be rewritten as

$$m_P C\frac{dT_P}{dt} = \pi Nu_P k_g d_P(T_P - T_\infty) \tag{13}$$

where Nu_P is the particle local Nusselt number proposed by Hwang and Chang (1988) which is given by

$$Nu_P = \frac{Nu_0}{1+3.42\left(\frac{M_P}{\mathrm{Re}_P\mathrm{Pr}}\right)Nu_0} \tag{14-1}$$

$$Nu_0 = 2.0 + 0.6\mathrm{Re}_P^{0.5}\mathrm{Pr}^{0.33} \tag{14-2}$$

where Nu_0 is the Nusselt number of a free falling droplet. The gas Prandtl number (Pr) is defined by

$$\mathrm{Pr} = \frac{\mu C_P}{k_g} \tag{15}$$

Up to here, only the gas phase effects on the particles are regarded. For treating the two-way coupling whereby the dispersed phase also affects the continuous phase through the interphase momentum and thermal coupling, the source vector of **S** in the Eq. (1) should be replaced appropriately to consider the particles effects on the gas medium. The net difference of mass, momentum and energy of particles, entering and/or leaving each control volume, determine the source terms in the momentum and energy governing equations of carrier phase. The continuity equation does not change because the total mass of particles remains constant. The appropriate source terms for the momentum and energy equations are written in the following forms for each cell of the computational domain.

$$S_{pu} = \sum_{i=1}^{NTP}\left(\dot{m}_P u_P|_{incell} - \dot{m}_P u_P|_{outcell}\right)_i \tag{16}$$

$$S_{pv} = \sum_{i=1}^{NTP}\left(\dot{m}_P v_P|_{incell} - \dot{m}_P v_P|_{outcell}\right)_i \tag{17}$$

$$S_{ph} = \sum_{i=1}^{NTP}\left(\dot{m}_P h_P|_{incell} - \dot{m}_P h_P|_{outcell}\right)_i \tag{18}$$

In these formulations, S_{pu} and S_{pv} are the corresponding source terms to the momentum equations respectively in the x- and y-directions, S_{ph} represents the energy source term, NTP is the number of trajectories of particles, $\dot{m}_P$ is the particle mass flow rate on each trajectory, u_P and v_P are the particle velocity components, and h_P is the enthalpy of particle moving along each trajectory. Within each time step, the above summations are taken over the particle trajectories to calculate the source terms of carrier phase at each control volume. This process is continued until the particles effect on the gas phase and vice versa reaches the minimum extent satisfying the convergence criterion. The enthalpy of each particle is obtained by the following relation.

$$h_P = aT_P + \frac{1}{2}(b\times10^{-3})T_P^2 + \frac{1}{3}(c\times10^{-6})T_P^3 - \frac{d\times10^5}{T_P} - A + (h_P)_{298\ \mathrm{K}} \tag{18-1}$$

where a, b, c, d and A are constants that depend onto the material of particles (Weast et al., 1985).

3. Numerical simulation

3.1. Grid generation, B.C. and I.C. impositions

More accurate and realistic simulation of the separation phenomenon is achieved by the consideration of nozzle external stream. For this purpose and to accelerate the solution convergence, a structured multiblock computational domain is prepared to solve the flow governing equations in such complex flow geometry. The structured grids within the blocks allow high computational efficiency and numerical accuracy of the results. Continuous grids between the blocks are the simplest and most convenient to deal with. With continuous grids, it is easy to guarantee the conservation across the block interfaces, achieve high numerical accuracy, and apply the efficient solution methods. In a multiblock system, each topological element has its own local coordinate system. The parameterization of the curve of an edge or the surface of a face defines a local coordinate system in that edge and face. The unit square for face and the unit interval for edges can always be used as the range of the local coordinates. The successful use of block-structured-grid-based methods for solving viscous flows over complex aerodynamic configurations has been demonstrated in the literatures (Arcill et al., 1991; Choo, 1995; Smith, 1992; Weatherill, 1990, 1994; Weatherill et al., 1994). An excellent and general overview about multiblock grids can be found in Dannenho_er (1994), Vatsa et al. (1995).

The close-up view of nozzle grid distribution is illustrated in (Fig. 1). The third-order polynomial determining the nozzle contour is also appended to the figure. The grids covering half of the computational domain are generated through three blocks. Blow-up of the domain decomposition and multiblock grids are shown

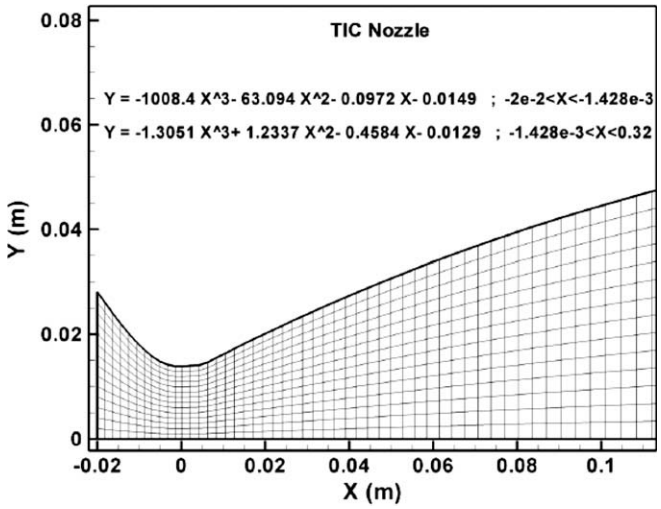

Fig. 1. Multi-block grid generation for the computational domain involving TIC nozzle and external stream.

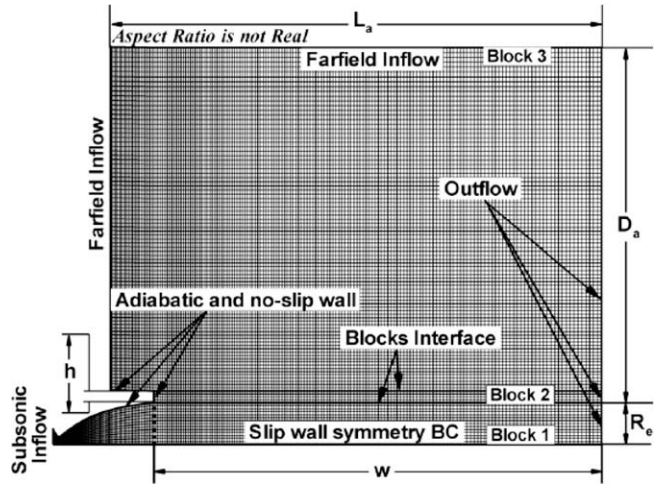

Fig. 2. Dimensions of computational domain, and imposed boundary conditions.

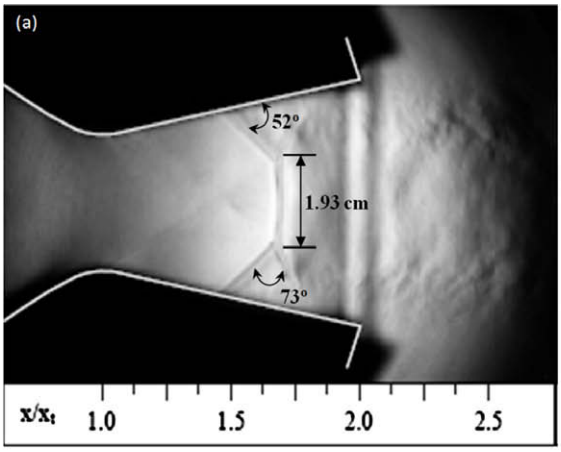

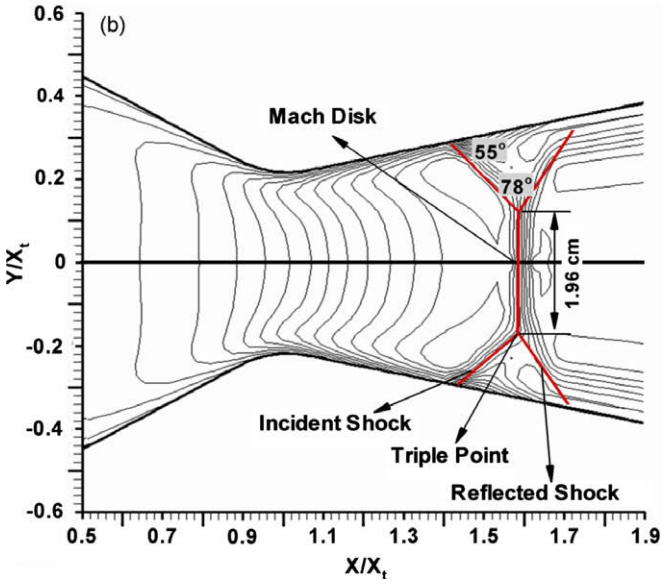

Fig. 4. Mach number disk diameter and the lambda shock structure angles at NPR = 2.4: (a) Schlieren flow visualization for 2D-CD nozzle, photographed by C.A. Hunter (Hunter, 1998), NASA Langley Research Center, Hampton, Virginia; (b) present computation.

in (Fig. 2). The two-dimensional domain for the TIC nozzle includes the full *X* dimension and half of the *Y* dimension. The parameter R_e represents the radius of the nozzle exit which is addressed to determine the other dimensions of the computational domain. The Block 1 is extended from 0.27 R_e upstream of the throat to the right face of the main domain. The external length (*W*) of the

	Coordinates (m)	
Point	X	Y
A	0.000	0.000
B	0.000	-0.0154
C	0.000	0.0347
D	0.0229	0.0291
E	0.0497	0.0153
F	0.0599	0.0138
G	0.0608	0.0140
H	0.0569	0.0292
I	0.1138	0.0243

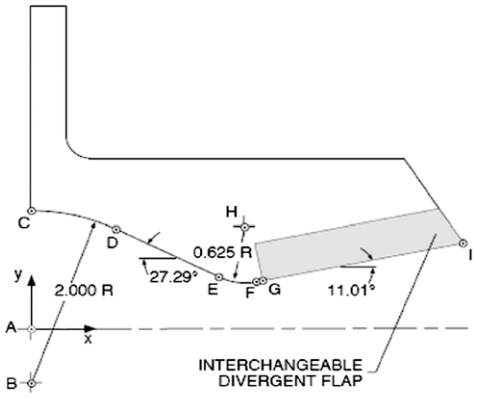

Fig. 3. Schematic of 2D-CD nozzle used as a benchmark for code validation (Hunter, 1998).

Block 1 is set to 21.5 R_e to account for the dissipation of oscillating shear layer created between the exit jet and external stream. The neighbor zone entitled by Block 2 has a height (h) equal to 0.25 R_e that is chosen small enough to capture fine vortices generated by the ambient flow suction into the separated area. The Block 3 begins from 2.5 R_e downstream of the throat that is chosen big enough to simulate the ambient flow turning due to the suction of separation zone. This block has a length (L_a) equal to 23.6 R_e and a width (D_a) equal to 8.25 R_e. Meanwhile, for the Block 1, the number of 3360 nodes, 11 × 14 nodes for the convergent part, 80 × 14 nodes for the divergent part, and 149 × 14 nodes for the rest, are considered. Block 2 consists of 148 nodes in the streamwise direction and 5 nodes in the vertical direction. In the Block 3, 174 nodes in the streamwise direction and 87 nodes in the vertical direction are distributed. In order to satisfy the grid-independent solution, several grid resolutions were tested. Aforesaid grids were selected as the most efficient resolution when a finer mesh with 20% extra nodes yielded a maximum difference of 1.02% in the velocity and temperature profiles plotted in several sections along the computational domain.

3.2. Numerical procedure

The physical space is transformed to a computational space in order to promote the numerical efficiency, and apply the physical boundary conditions conveniently using the following coordinates transformation.

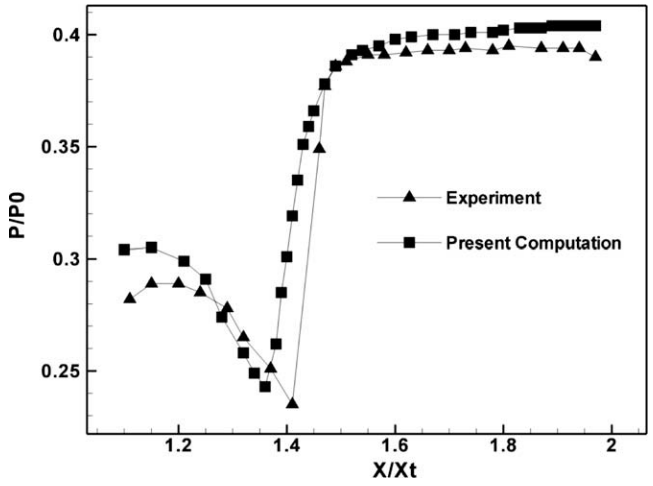

Fig. 5. Graphical comparison of Hunter's experimental wall pressure (Hunter, 1998) and present computation, Overexpanded 2D-CD nozzle at NPR = 2.4.

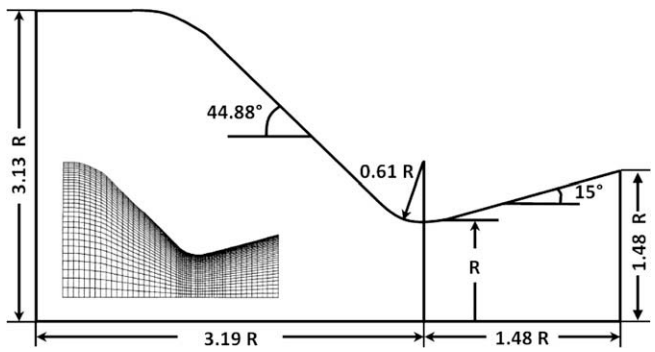

Fig. 6. Schematic sketch of JPR nozzle used for code verification (Mehta and Jayachandran, 1998) appended with the grid topology used.

$$\xi = \xi(x,y), \quad \eta = \eta(x,y) \tag{19}$$

After the coordinates transformation, the Eq. (1) becomes

$$\frac{\partial \hat{\mathbf{Q}}}{\partial t} + \frac{\partial}{\partial \xi}(\hat{\mathbf{F}} - \hat{\mathbf{F}}_v) + \frac{\partial}{\partial \eta}(\hat{\mathbf{G}} - \hat{\mathbf{G}}_v) = \hat{\mathbf{S}} \tag{20}$$

where

Table 2
Two-phase flow input data for JPL nozzle (Mehta and Jayachandran, 1998).

Gas phase (air)	Particle phase (alum. oxide)
P_0 = 1.0342 Mpa	C = 1380.0 J kg^{-1} K^{-1}
T_0 = 555.0 K	ρ_P = 4004.62 kg/m^3
γ = 1.4	d_P = 5 μm
C_P = 1070.0 J kg^{-1} K^{-1}	ϕ = 0.3
Pr = 0.74	

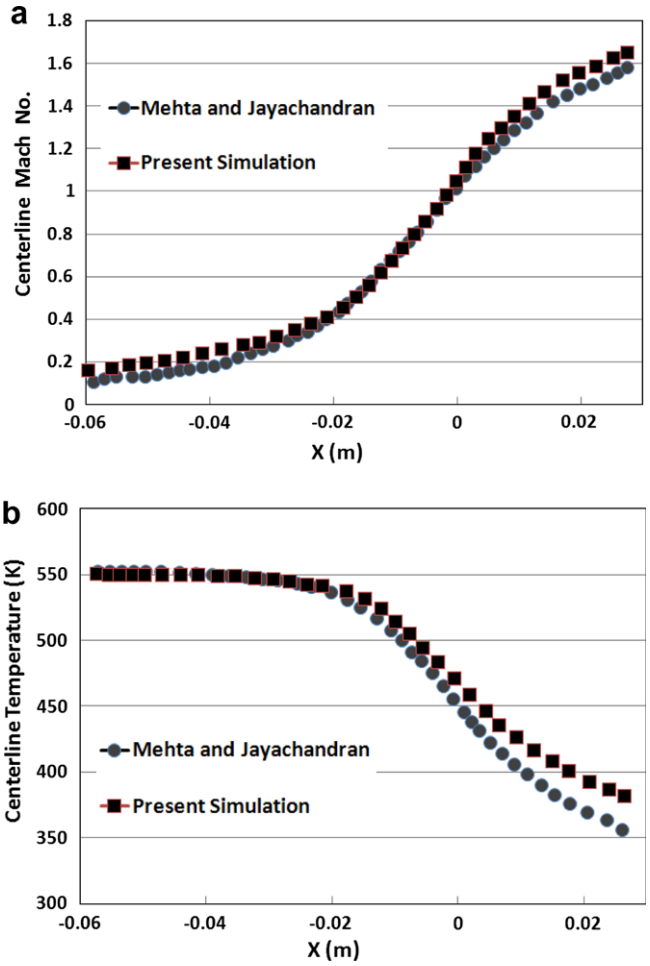

Fig. 7. Comparison of present simulation and (Mehta and Jayachandran's results, 1998) for a JPR nozzle: (a) the centerline Mach number distribution; (b) the centerline temperature distribution.

Table 3
Three kinds of two-phase flows simulated in the TIC nozzle.

	Particles Diameter (μm)	Particles mass flow Rate (kg/s)/fraction (%)
Case I	1	1.122/8.5
Case II	5	1.122/8.5
Case III	5	1.848/14

$$\hat{\mathbf{Q}} = J^{-1}\mathbf{Q}, \quad \begin{Bmatrix} \hat{\mathbf{F}} \\ \hat{\mathbf{G}} \end{Bmatrix} = J^{-1} \begin{Bmatrix} \xi_x \mathbf{F} + \xi_y \mathbf{G} \\ \eta_x \mathbf{F} + \eta_y \mathbf{G} \end{Bmatrix},$$
$$\begin{Bmatrix} \hat{\mathbf{F}}_v \\ \hat{\mathbf{G}}_v \end{Bmatrix} = J^{-1} \begin{Bmatrix} \xi_x \mathbf{F}_v + \xi_y \mathbf{G}_v \\ \eta_x \mathbf{F}_v + \eta_y \mathbf{G}_v \end{Bmatrix} \tag{21}$$

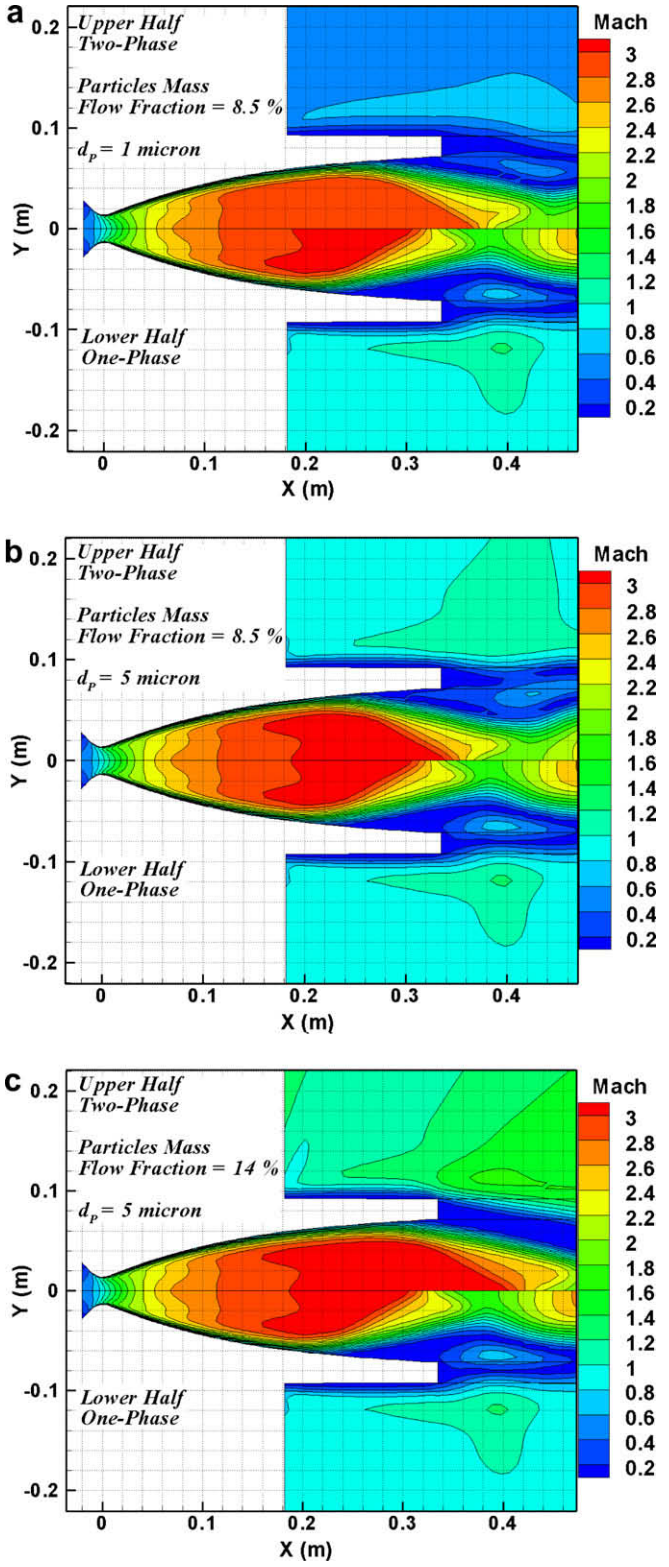

Fig. 8. Comparison of Mach number contours between three studied two-phase flows and the reference one-phase flow: (a) Case I; (b) Case II; (c) Case III.

Here, J is the transformation Jacobian $(\xi_x\eta_y - \eta_x\xi_y)$ that represents the volume of each cell in the Cartesian coordinates system.

A node-based algorithm in which the variables are stored at the vertices is used, and the equations are solved in non-overlapping control volumes surrounding each node. A fully implicit finite volume method is implemented on the present multiblock spatial domain. The convective flux terms are formulated using the van Leer's flux-splitting scheme (Van Leer, 1982), and MUSCL type variable extrapolation approach is used to get a high-order spatial accuracy and the TVD property. The MUSCL approach extends the spatial accuracy to second order and is combined with minmod or van Albada's gradient limiters to ensure monotonicity across discontinuities such as shock waves to make the solution stable. This approach is fully necessary to prevent numerical instabilities in the shock regions, especially in particular for nozzle cases.

The van Leer's procedure enhances the robustness of the computer code and maintains the desirable characteristic of Roe's scheme to capture discontinuities with one or two grid points. Both methods (Van Leer and Roe) implement the finite volume princi-

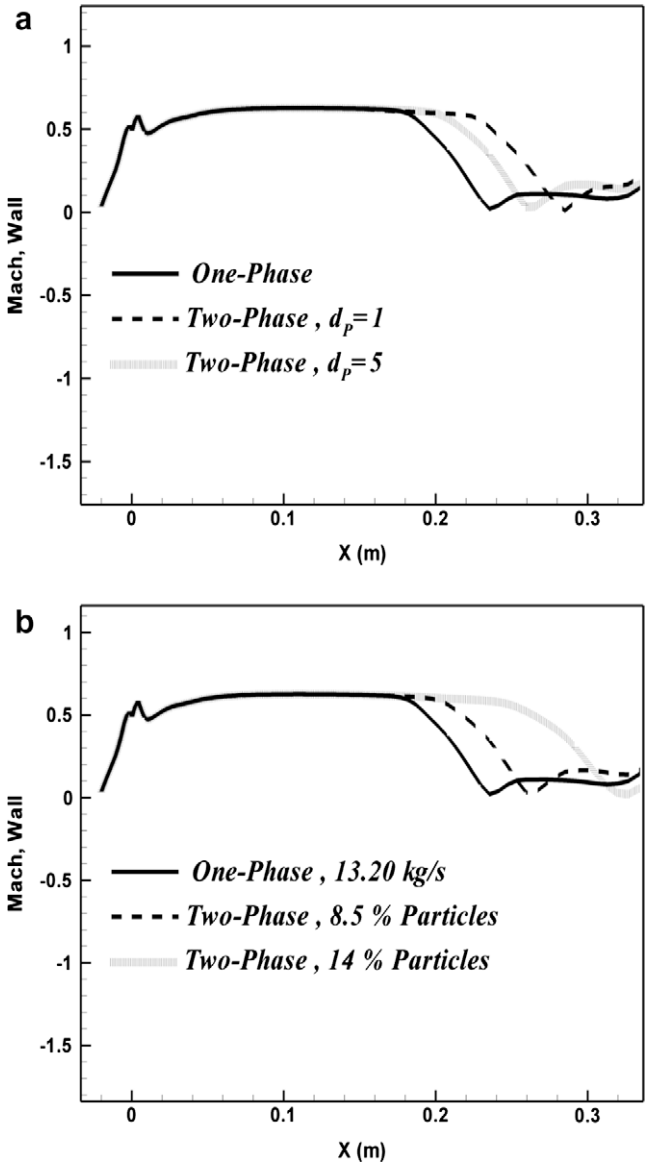

Fig. 9. Distribution of Mach number at the nozzle near-wall region: (a) diameter-based comparison at particles mass flow fraction of 8.5%; (b) mass flow rate-base comparison at particles diameter of 5 μm.

ples to balance the fluxes across the cell faces, and determine the fluxes at the cell interfaces. Only the inviscid terms of the flux vectors are split and upwind differenced, whereas the diffusion terms of the Navier–Stokes equations are centrally differenced (Abdol-Hamid, 1991; Van Leer, 1982; Roe, 1986). The scheme is spatially third-order accurate while at the discontinuities its accuracy reduces to the first order. Fully implicit time integration method is used for analysis of supersonic non-reacting flow by applying the LU-SSOR method proposed by Shuen and Yoon (1988). Pseudo-time iterations are used to obtain the steady-state solution.

3.3. Turbulence modeling

Depending on the particular flow case involving both attached and detached near-wall flows, we have used the modified form of the well-known two-layer algebraic Baldwin–Lomax (B–L) model Baldwin and Lomax, 1978 to calculate the turbulence dissipation. The original model was modified by Degani and Schiff (1983) to determine the outer length scale more accurately when a strong vortical flow structure or a massive separation exists. The successful simulation of detached flows using the modified B–L turbulence model is case-dependant. Here, reasonable agreement of the present work with the experiment (as will be discussed in the Section 4) made us certain about a good choice of an accurate and economic turbulence model, and the rightness of model coefficients was justified. In this model, the flow governing equations are changed to the Reynolds-Averaged ones. By implementing the 2D boundary layer simplifications, Boussinesq (White, 2006) approximation relates the Reynolds stresses to the mean velocity gradient through a parameter named turbulent viscosity. The zero-equation model used herein evaluates this parameter appropriately. More details can be found in Baldwin and Lomax (1978) and Degani and Schiff (1983).

4. Model validation

The performance of the prepared CFD code in both single- and two-phase benchmark flows is verified respectively against experimental and numerical data. The single-phase simulation is validated using the Hunter's experiment (Hunter, 1998) in a two-dimensional convergent–divergent (2D-CD) nozzle. The numerical simulation of Mehta and Jayachandran (1998) of a gas–solid two-phase flow in a JPR nozzle is employed to verify the two-phase flow simulator code.

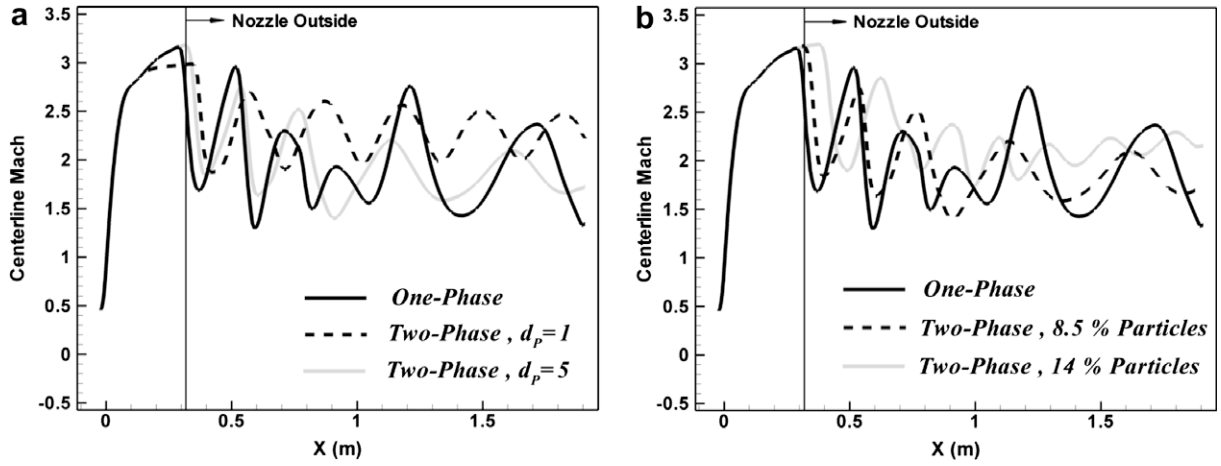

Fig. 10. Distribution of centerline Mach number inside and outside the nozzle: (a) diameter-based comparison at particles mass flow fraction of 8.5%; (b) mass flow rate-base comparison at particles diameter of 5 μm.

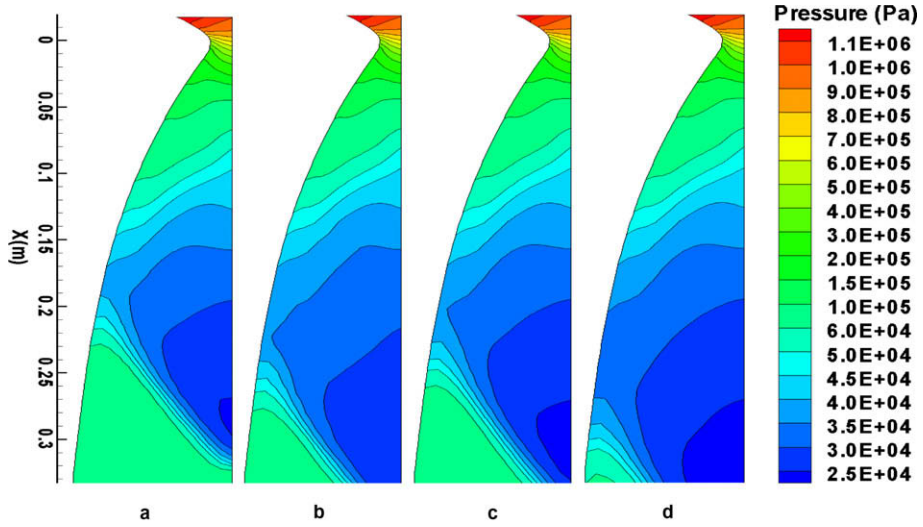

Fig. 11. Comparison of pressure contours between three studied two-phase flows and the reference one-phase flow: (a) one-phase; (b) Case I; (c) Case II; (d) Case III.

4.1. Single-phase flow

To ensure the validity and accuracy of the employed numerical procedure, a rigorous comparison between present computation and Hunter's (1998) experiment conducted for a 2D-CD nozzle in pressure ratio of 2.4 is implemented. The test nozzle used in his investigation is a subscale, non-axisymmetric, two-dimensional convergent–divergent (2D-CD) nozzle with a throat nominal area of $A_t = 2.785 \times 10^{-3}$ m^2, an expansion ratio of $A_e/A_t = 1.797$. Geometric details of 2D-CD nozzle are shown in (Fig. 3).

Fig. 4 comprises a well defined lambda shock structure and a FSS that begins at the leading lambda shock and extends downstream. The abscissa is normalized by the throat position (x_t) measured away from the nozzle inlet. The diameter of Mach number disk and the measure of two angles, one between the nozzle wall and oblique shock and the other between the oblique and reflected shocks are designated as the comparison criteria. The part (a) of the figure represents the Schlieren flow visualization at NPR = 2.4 photographed by Hunter (1998), and the part (b) shows the present work. A reasonable correspondence (with maximum relative error less than 6.8%) between the experiment and present computation through these parameters was achieved.

A comparison between the computed and experimental dimensionless wall pressures plotted as a function of normalized distance is diagrammed in Fig. 5. Pressure is non-dimensionalized by chamber stagnation pressure (P_0). The separation occurs at $x/x_t = 1.37$ which is only 2.8% different from the experimental prediction ($x/x_t = 1.41$). Also, the dimensionless pressure in numerical solution is 2.5% different from the experiment at the point of separation commencement. There is a minor difference between numerical and experimental results because of the assumption of 2D symmetric geometry even though the experiment was performed in the non-axisymmetric three-dimensional nozzle. The pressure peak observed in (Fig. 5) justifies the formed separation,

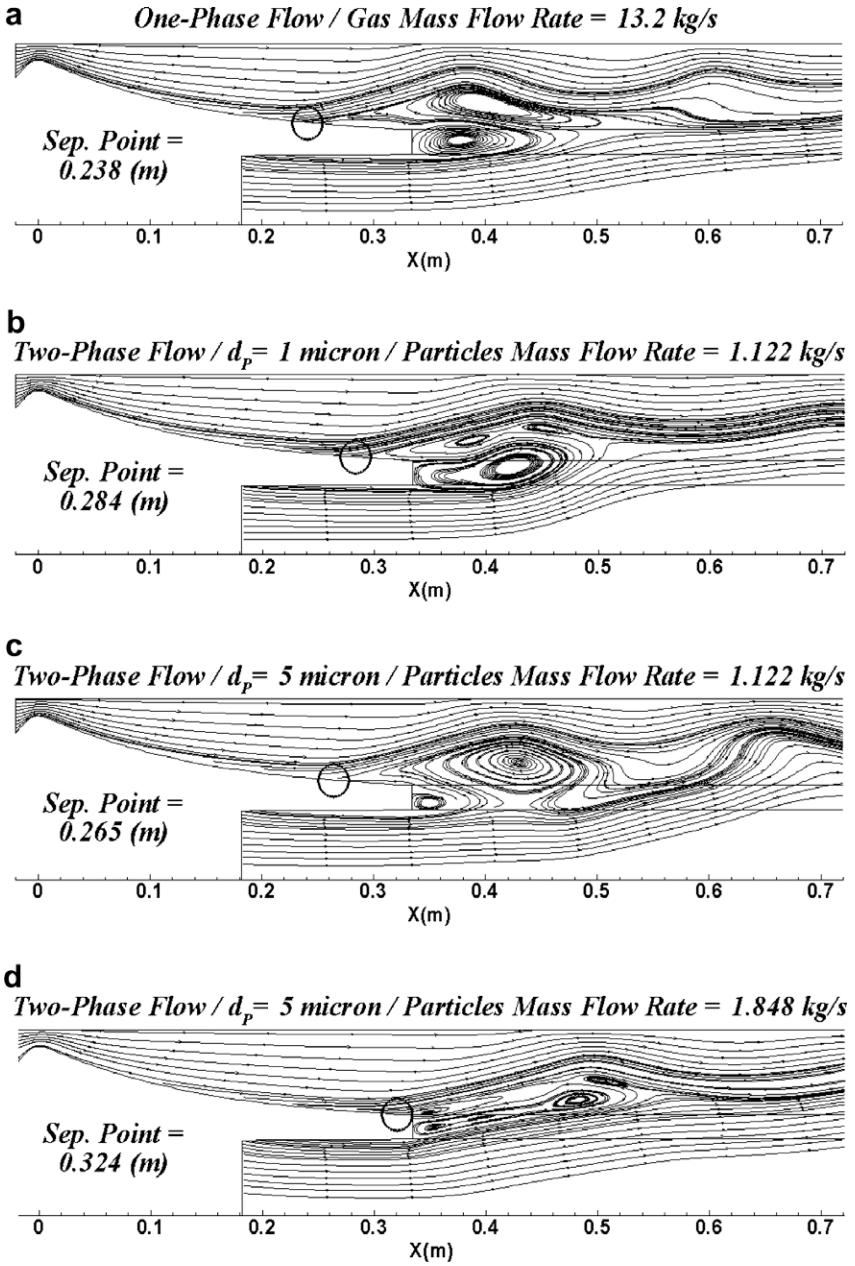

Fig. 12. Streamlines of the reference one-phase flow and three studied two-phase flows: (a) one-phase flow; (b) Case I; (c) Case II; (d) Case III.

its accompanied oblique shock, and the existence of adverse pressure gradient. An acceptable agreement between the present computation and Hunter's experiment is also observed in the nozzle wall pressure.

4.2. Coupled two-phase flow

To check the capability of adopted Eulerian–Lagrangian numerical procedure to simulate the coupled two-phase nozzle flows, the Mehta and Jayachandran's numerical study (Mehta and Jayachandran, 1998) is chosen as a benchmark for code verification. They developed a fast numerical algorithm to solve the two-phase viscous flow in an axisymmetric convergent–divergent nozzle with employment of a simple structured grid arrangement. An Eulerian–Eulerian approach with appropriate exchange terms for gas–particle interaction was used to simulate the coupled gas–particle flow in a Jet Propulsion Laboratory nozzle. Turbulence closure was treated using the algebraic Baldwin–Lomax model. Their simulation was compared with experimental data, and reasonable agreement was achieved. The geometry of JPR nozzle is depicted in (Fig. 6). The nozzle dimensions are all indicated using the throat radius (R). The physical attributes of gas–particle flow are given in the (Table 2). The carrier phase is the air, and the aluminium oxide particles are the dispersed phase. The parameter ϕ denotes the ratio of particles mass flow rate to the gas one. The particles are also distributed uniformly at the inlet of the nozzle.

Mach number and temperature distributions along the JPR nozzle centerline are presented respectively in Fig. 7a and b. The parameter X(m) is measured away from the throat. A reasonable correspondence between the Mehta & Jayachandran's results, (1998) and present simulation is discernable. Maximum difference percentage between two works is 3.9% in Fig. 7a and 5.8% in Fig. 7b.

5. Results and discussion

The particles material is assumed to be the aluminium oxide. It has a close practical relation to the aerospace applications such as solid rocket engine in which aluminum particles are used to reduce the vibration due to the instability. The described truncated ideal contour nozzle (Section 3.1) is utilized during this study. The TIC nozzle in the overexpanded regime contains the Free Shock Separation (FSS). Flow turning losses associated with the flow separation, or internal shock wave interference may reduce the nozzle effectiveness. The carrier phase is assumed to be the hot air coming out from the combustion chamber at 3200 K, 114.5 kPa, the stagnation pressure of 1145.0 kPa, and the Mach number of 0.8 that produces a mass flow rate of 13.2 kg/s. The gas constant (R) is equal to 0.287 (kJ/kg K). The specific heat (C), density (ρ_P) and diameter (d_P) of particles are also taken according to the (Table 2). The single-phase flow of this working fluid is simulated separately and is taken as a reference case or representative of a single-phase flow during the comparison with other studied two-phase flows. The particles are distributed uniformly at the inlet. Two different particle diameters (1 and 5 μm), and two particle mass flow rates (1.122 and 1.848 kg/s) are studied and compared. The three studied two-phase flows are addressed throughout the paper using the Greek numbers as shown in the (Table 3).

The aerodynamic and thermal effects of the particles on important parameters of the compressible two-phase flows are discussed separately. A general study on the dispersion of solid particulates inside and outside of the nozzle is also presented. The gas and the particles are initially supposed to be in a state of thermodynamic and kinematic equilibrium. Apparently, the particle phase brings about some prominent variations in the flow kinematic, thermal and physical properties. Here, the major effort is focused on a quantitative demonstration of these variations through the comparison of Mach number, pressure and temperature contours, flow streamlines, velocity, temperature and Mach number distributions and the separation point (SP) transition in different cases studied here.

5.1. Comparison of one- and two-phase separated flows

5.1.1. Aerodynamic comparison

The Mach number contours are compared between the reference one-phase flow and the three studied two-phase flows in (Fig. 8). The Mach number contour of the Cases I–III (according to the Table 3) are presented in (Fig. 8a–c) respectively. Lower half represents the Mach number contours of the one-phase reference flow, and the upper half represents one of the two-phase cases. Particles mass flow fraction (the ratio of mass flow rate of particles to gas), and the diameter of particles exist in the combustion products are all indicated in the figures.

Comparing the two- and one-phase flows in Fig. 8a and b, it can be observed that the local Mach number is increased when the bigger particles are released into the field. As was noted, the particles are in dynamic equilibrium with the carrier phase at the inlet. Bigger particles (5 μm) carry more values of momentum than do the smaller ones (1 μm), so more momentum is transferred to the carrier phase and the local gas velocity (Mach number) increases.

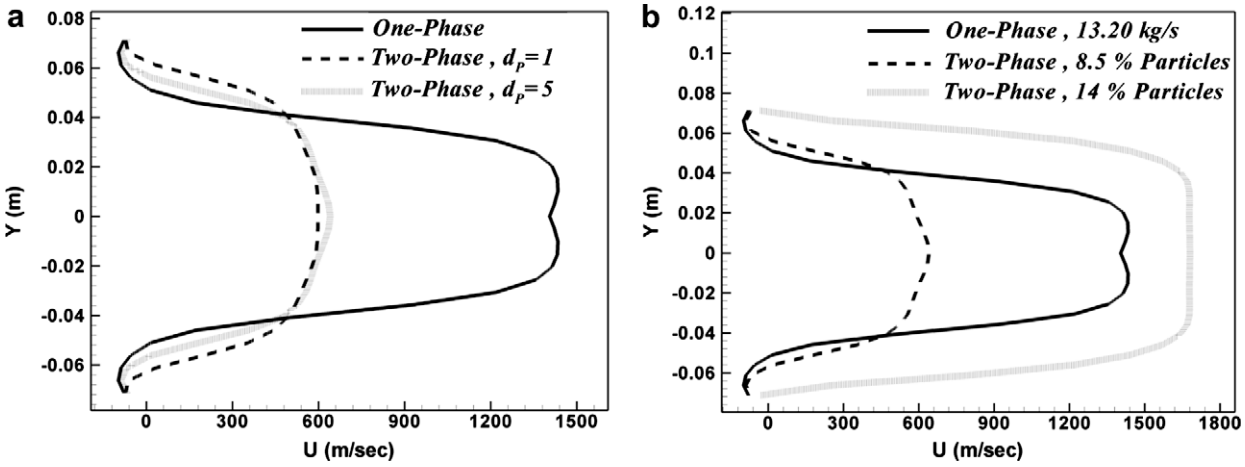

Fig. 13. Comparison of gas velocity profiles at the nozzle exit; (a) diameter-based comparison at particles mass flow fraction of 8.5%; (b) mass flow rate-base comparison at particles diameter of 5 μm.

Particles are the elements carrying energy signals between the continuous and discrete phases. In a two-way exchange of energy, it is hard to determine the actual direction of energy transfer between the dispersed and carrier phases without the assistance of numerical results. More particles within the flow yield more dispersion in the field than do the fewer ones. Therefore, more changes in the carrier phase properties are brought about. Comparing Fig. 8b and c proves this issue, and reveals that the increment of the particles mass flow fraction (or particles number) increases the extent of changes in the Mach number contours. In the supersonic zone next to the centerline, the supersonic zone is extended diffusively as the particles number increases. More diffusion of particles into the carrier phase increases the net density of gas phase (if we assign an individual averaged density to the gas–solid flow) and therefore the separation delays eminently because of the increased momentum of the gas–solid flow.

The maximum local Mach number in the nozzle for the reference one-phase flow is approximately equal to 3.15 while for the Cases I–III it amounts to 2.99, 3.18 and 3.215, respectively. These values show that the particulates exist in the combustion products may increase or decrease the Mach number and velocity of carrier phase that this is highly depended to the particles diameter and mass flow fraction. Comparing these values indicates that in a two-phase regime the increment of particle mass flow fraction and particle diameter increase the maximum local Mach number.

The Mach number distribution at the nozzle near-wall region is diagrammed in the (Fig. 9) for the cases studied. Part (a) of the figure demonstrates a comparison between studied one- and two-phase flows based on the particles diameters at constant particles mass flow fraction of 8.5%, and the part (b) shows this comparison based on the particles mass flow rate at constant particles diameter of 5 μm. The near-wall Mach number as can be observed from the Mach number contours (Fig. 8) remains approximately unchanged for all cases before the separation point. Abrupt Mach number decrement represents the separation point position at the studied cases. Regarding (Fig. 9), the smaller particles delay the separation, and the lower particles mass flow fractions advance the separation. In the near wall is there a strong backflow coming from the separation phenomenon. This moves the inflection point of the velocity profile toward the wall until it reaches the nozzle contour, and the velocity (or local Mach number) of flow considerably reduces at the near-wall region. This can proves the approximate zero Mach number (or gas velocity) at this region after the appearance of separation point.

The centerline Mach number variations inside and outside the nozzle are also depicted in (Fig. 10). Before the incidence of separation-accompanied shock wave to the centerline, the graphs coincide roughly each other, and after that the centerline Mach number reduces abruptly. The existence of particulates in all cases shifts downstream the point of shock incidence to the axis. The bigger particles compel the oblique shock to interact sooner with the centerline, or in the other word, the shock system appearance and its accompanied separation delays by the smaller particles. The increment of particles diameter and mass flow rate increase the maximum attainable Mach number by the flow inside the nozzle. This shows that the effect of particles on the acceleration of centerline gas inside the nozzle is prominent. This is the main benefit of a two-way coupled simulation that is able to capture the considerable effects of the dispersed phase on the carrier one. The centerline Mach number starts to oscillate when encounters the wavy flow patterns produced by the interaction of nozzle exit jet and external stream. Focusing on the diagrammed oscillatory behavior reveals that the net amplitude of Mach number oscillations reduces as the particles are considered in the simulation.

A comparison of the nozzle pressure contours between the reference one-phase and the three studied two-phase flows is given in (Fig. 11). The minimum local pressure moves toward the nozzle exit when the additional phase (solid particulates) is considered in the simulation. This means that the particle phase has a direct effect on the oblique shock position, separation point transition,

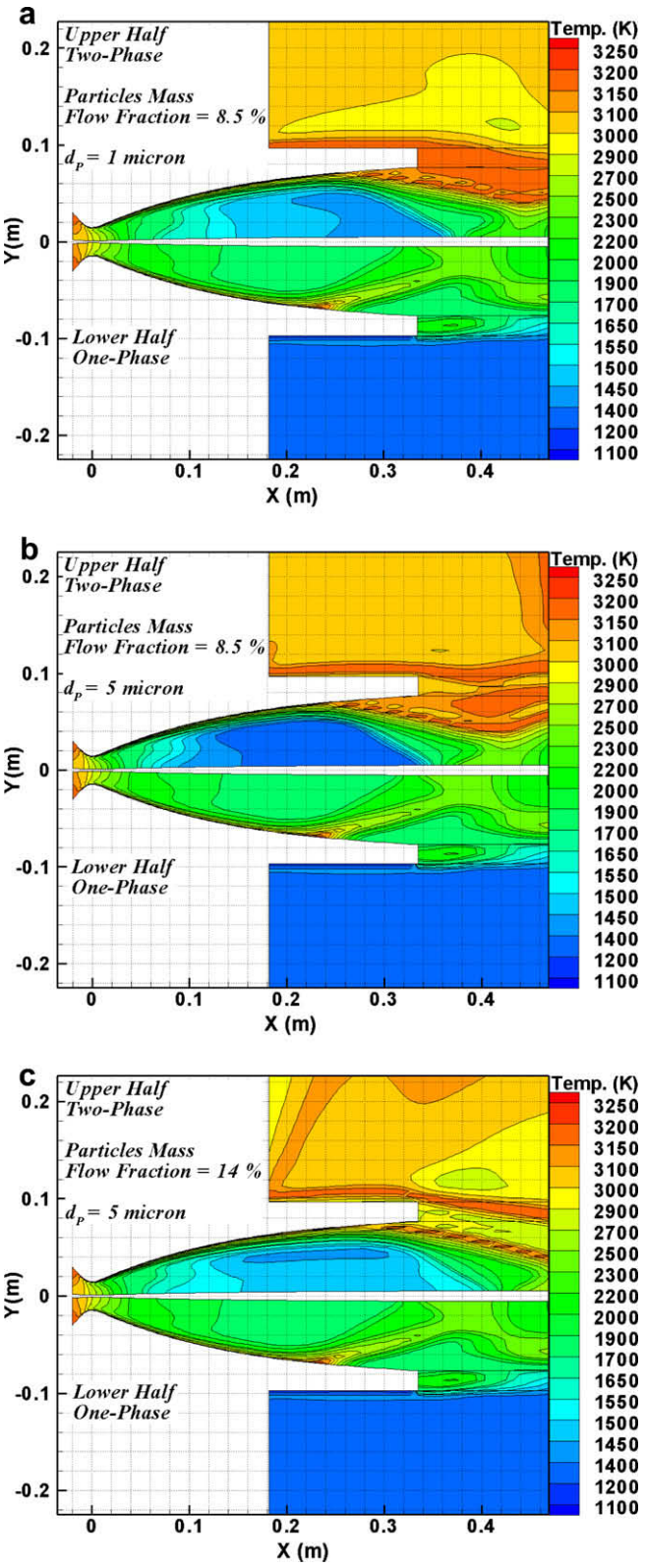

Fig. 14. Comparison of temperature contours between three studied two-phase flows and the reference one-phase flow: (a) Case I; (b) Case II; (c) Case III.

the extent of the separated area, the intensity of suction of the separated area and etc. In a definite single-phase compressible flow, the shock waves are formed in order to produce large gradients in flow properties to adjust the nozzle internal and external conditions. The existence of particulates, as it will be shown later, delays eminently the separation point and its accompanied shock wave. One can readily calculate the net pressure loss along the nozzle by looking into the pressure contours pattern right at the nozzle exit. Regarding the fact that the one- and two-phase flows condition at the nozzle inlet are all identical, lower averaged pressure at the nozzle exit determines the case in which we have more pressure loss along the nozzle. If we arrange the studied cases according to this criterion, the non-equality of Case III > Case II > Case I holds for the amount of pressure loss along the nozzle. Meanwhile, it is apparent that the existence of solid particulates hinders the flow of carrier phase and therefore leads to higher pressure loss.

The flow streamlines for the studied cases are plotted in (Fig. 12). The separation point position (main output of the present study) and the characteristics of the studied cases are indicated in the figures. The separation point, its accompanied oblique shock wave and the vortical structures of the flow formed behind the separated area move downstream as the particulates are considered in the simulation. Allowing the particles into the nozzle increases the pressure loss along the nozzle (see Fig. 11) and therefore the suctional power of the separated area increases. The number and pattern of flow vortices, their net angular velocity and net area vary as the particles diameter and mass flow rate change. A simple comparison between the streamlines reveals that as the separation point travels downstream, more distortion in the flow vortical patterns obtains. Referring to the part (a) of this figure (SP = 0.238 m) where both of vortices behind the separated area are roughly similar, the vortex next to the exit lip which has been entrapped by the ambient turning flow gets smaller as the separation moves a little downstream in (Fig. 12c) (SP = 0.265), while the upper vortex formed between the nozzle main stream and turning suction flow gets bigger. More transition of the separation point toward exit in (Fig. 12b) (SP = 0.284) enlarges the entrapped vortex, and crashes down the upper one into two single smaller vortices. Consequently, in the part (d) of the figure (SP = 0.324) where the separation occurs near the exit lip, the entrapped vortex crashes down into two separate vortices, and the maximum distortion in flow vortical patterns appears. The carrier phase momentum energy debilitates when it declines toward the dispersed solid phase. This happens when the bigger particles produce greater negative momentum energy source terms in the Eqs. (16) and (17) that eminently absorb the gas momentum. The decrement of fluid momentum weakens it against the positive pressure gradient, and therefore the separation advances in the (Fig. 12c). A converse deduction holds for the smaller particles and the delay of separation. At the end, the gas velocity profile at the nozzle exit is compared between the studied one- and two-phase flows in (Fig. 13).

5.1.2. Thermal comparison

Temperature contours are compared between the reference one-phase and three studied two-phase flows in (Fig. 14). Regarding the three parts of the figures, the difference between the temperatures of the nozzle inside and ambient decreases when the particulates are considered in the simulation. It can be inferred from the figure that the particles reduce the gas local temperature in the nozzle divergent part. The carrier phase is the only element of this flow which can sense the expansion effects coming from the nozzle divergent part. In reply to this expansion, the temperature decreases eminently in this region. A part of the released heat transfers to the particles until their heat capacity gets saturated. To satisfy the thermal energy balance throughout the computational domain, the ambient temperature should be increased more

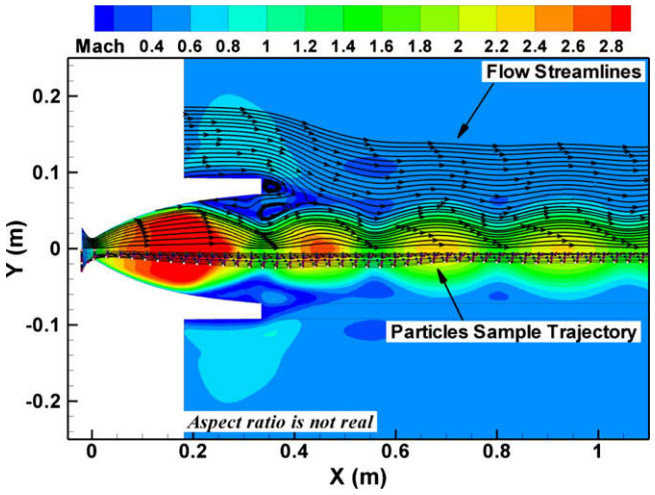

Fig. 16. The interaction of nozzle exit jet streamlines with ambient shown for the one-phase reference case.

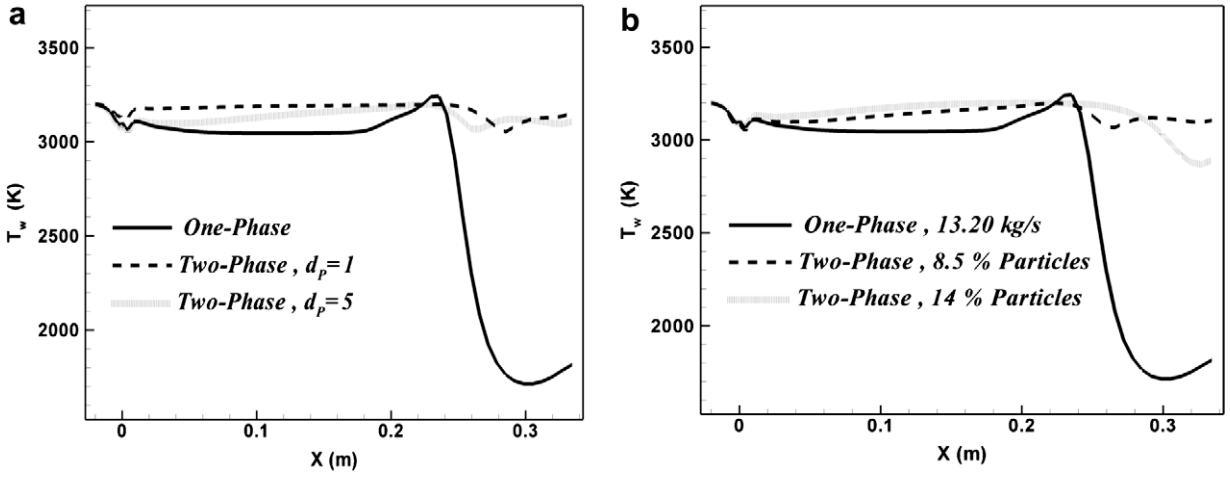

Fig. 15. Distribution of temperature at the nozzle near-wall region: (a) diameter-based comparison at particles mass flow fraction of 8.5%; (b) mass flow rate-base comparison at particles diameter of 5 μm.

than what is expected and observed in the one-phase reference flow. In two-phase cases, the metallic particulates play their role as a thermal sink in the way that gas can easily be expanded and cooled in the divergent part.

The gas temperature at the nozzle near-wall region is compared between the cases studied, and demonstrated in (Fig. 15). After experiencing the separation, the carrier phase reacts disparately to this phenomenon. This reaction inherently depends upon to the particles momentum and thermal response times. The net thermal response time is approximately 44% greater than the net momentum response time throughout the computational domain. This confirms that transferring the thermal signals between the carrier and dispersed phases takes longer than momentum signals. Comparing the Mach number (Fig. 8) and temperature (Fig. 15) distributions at the nozzle wall approves this matter. For all cases studied, the abrupt reduction of wall Mach number (that comes from the separation-accompanied shock wave) occurs consecutively inside the nozzle, while for the wall temperature, this abrupt reduction does not occur inside the nozzle for the two-phase cases studied. This comes back to the aforementioned 44% greater delay exists in transferring the thermal energy signals between two phases which brings about later adoption between two phases thermal conditions. If the nozzle geometry was longer a little than what is now, it would be possible to capture the wall temperature abrupt reduction for two-phase cases inside the nozzle. Meanwhile, the maximum attainable wall temperature by the flow decreases in the presence of the second solid phase.

5.2. External stream and particles trajectory

We know from the laboratory experiments that the Kelvin–Helmholtz shear instabilities grow rapidly on the boundary of supersonic gas jets, and effectively decelerate and disrupt the flow. Crisscrossing (or diamond-shape) shock waves produced by the interaction of supersonic exit jet and the ambient are the most powerful mechanism to make a wavy shear layer. Supersonic gas jets are created in laboratories by allowing a highly compressed gas through a nozzle into the atmosphere or some other ambient gases (Michael and Karl-Heinz, 1985). Laboratory jets usually have the density ratios of $\rho_{jet}/\rho_{ambient} > 1$, and are in moderate Mach numbers $M < 3.0$ which all hold in the current study. Duo to the tri-dimensionality of the exit jet, an accurate and quantitative discussion on behaviors of the exit jet is not possible through a 2D simulation. Therefore, this section is devoted to a qualitative study on interactions between the nozzle exit jet and the external stream in order to clarify the correlation which exists between jet-induced oscillations and particles dispersion.

External flow oscillations leading from the exit jet and external stream interaction are illustrated in (Fig. 16). The jet net wavelength decreases when the wave travels downstream while its net diameter increases. Both behaviors are replies to the mixing of exit jet with external stream, and the role which the viscous and turbulent dissipations play. It is discernable that the jet streamlines follow the wavelike pattern of Mach number contours. It was also checked that a similar manner holds for streamlines against the x-velocity, pressure, density and temperature contours. A sample illustration of particles oscillatory motion outside the nozzle is also given in the lower half of (Fig. 16). Inside the nozzle, the particles paths do not show an oscillatory motion while such behaviors start right after the nozzle exit. Particles trajectories oscillate when they expose to the crisscrossing shock waves generated outside the nozzle to approach the exit jet conditions to the ambient.

Sample trajectories are computed in a two-way manner to obtain the approximate paths the particles move along. Particles have been distributed uniformly at the inlet, and are in momentum and thermal equilibrium with the inlet gas. Particles sample trajectories inside the nozzle are shown in (Fig. 17). Particles considerable inertia enforces them to move close to the centerline, and an eminent particles-free zone is created near the nozzle contour. The

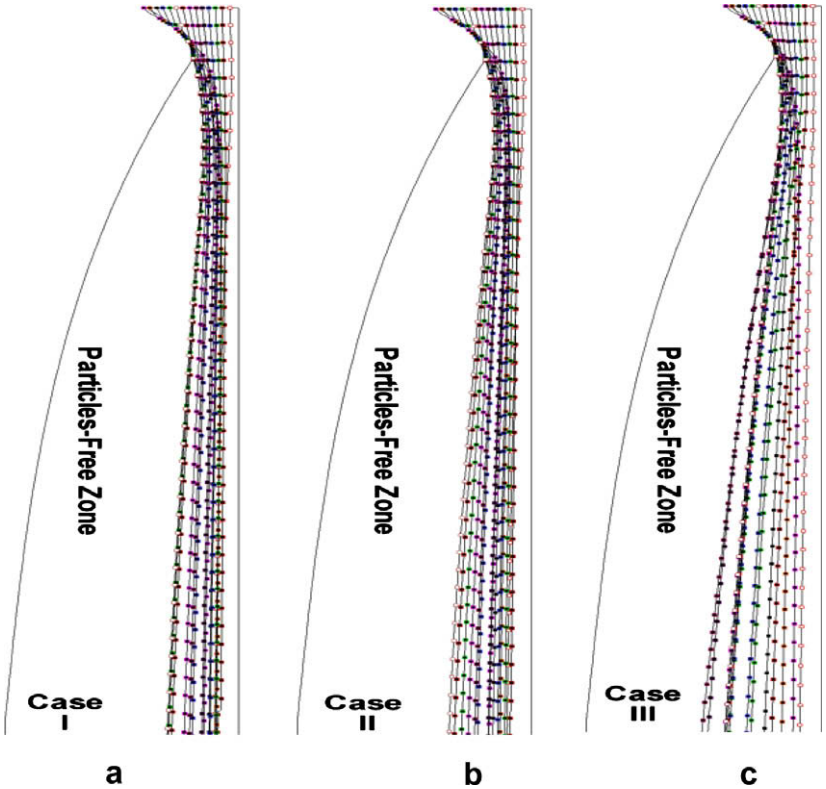

Fig. 17. Particles sample trajectories inside the nozzle for the two-phase cases studied: (a) Case I; (b) Case II; (c) Case III.

particles-free zone gets smaller as the particles diameter and mass flow fraction increases. This comes back to the increment of particles dispersion and the direct dependency it had with the particles diameter and mass flow fraction.

6. Conclusions

An Eulerian–Lagrangian approach involving a two-way momentum and thermal coupling between gas and particles exchanges was adopted to simulate the non-reacting dilute gas–solid flow in a TIC nozzle with consideration of external stream interactions. The main goal was to determine the separation point quantitatively and its variations versus the particles diameter and mass flow fraction. Based on the results presented, the following conclusions are drawn:

(1) The near-wall Mach number remains approximately unchanged for all cases before the separation point. After experiencing the separation, a prominent reduction in wall Mach number appears. These reductions occur consecutively inside the nozzle, and their arrangement corresponds to the order of points in those the separation occurs, because they are created in reply to the separation-accompanied shock wave. The supersonic zone next to the nozzle centerline extends diffusively as the particles number increases.

(2) The smaller particles delay the separation, and the lower particles mass flow fractions advances the separation. In the near wall is there a strong backflow coming from the separation phenomenon. This moves the inflection point of the velocity profile toward the wall until it reaches the nozzle contour, and the velocity (or local Mach number) of flow considerably reduces at the near-wall region. This can proves the approximate zero Mach number (or gas velocity) in the near-wall region after the appearance of separation point.

(3) Before the incidence of separation-accompanied shock wave to the centerline, the centerline Mach number diagrams coincide roughly each other, and after that they reduce abruptly. The existence of particulates in all cases shifts downstream the point of shock incidence to the axis. The bigger particles compel the oblique shock to interact sooner with the centerline, or in the other word, the shock system appearance and its accompanied separation delays by the smaller particles. The increment of particles diameter and mass flow rate increase the maximum attainable Mach number by the flow inside the nozzle. The centerline Mach number starts to oscillate when encounters the wavy flow patterns produced by the interaction of nozzle exit jet and external stream. Focusing on the diagrammed oscillatory behavior reveals that the net amplitude of Mach number oscillations reduces as the particles are considered in the simulation.

(4) The existence of particulates delays eminently the separation point, its accompanied shock wave and the vortical structures of the flow formed behind the separated area. The non-equality of Case III > Case II > Case I holds for the amount of pressure loss along the nozzle. Meanwhile, it is apparent that the existence of solid particulates hinders the flow of carrier phase and therefore leads to higher pressure loss, and therefore the suctional power of the separated area increases.

(5) The abrupt reaction of wall Mach number and temperature after separation inherently depend upon respectively to the particles momentum and thermal response times. The net thermal response time is approximately 44% greater than the net momentum response time throughout the computational domain. This confirms that transferring the thermal signals between the carrier and dispersed phases takes longer than momentum signals. To this reason, the abrupt reduction of wall temperature does not appear inside the nozzle for the two-phase cases studied. The maximum attainable wall temperature by the flow decreases in the presence of the second solid phase.

(6) Particles considerable inertia enforces them to move close to the centerline, and an eminent particles-free zone is created near the nozzle contour. The particles-free zone gets smaller as the particles diameter and mass flow fraction increases. Particles trajectories oscillate when they expose to the criss-crossing shock waves generated outside the nozzle to approach the exit jet conditions to the ambient.

References

Abdol-Hamid, Khaled S., 1991. Application of a multiblock/multizone code (PAB3D) for the three-dimensional Navier–Stokes equations. AIAA 2155.

Altman, D., Carter, J.M., 1956. Expansion processes. In: Lewis, B., Pease, R.N., Taylor, H.S. (Eds.), Combustion Processes. Princeton University Press, Princeton, NJ, pp. 52–60.

Arcill, A.S., Hauser, J., Eiseman, P.R., Thompson, J.F. (Eds.), 1991. Numerical Grid Generation in Computational Fluid Dynamics and Related Fields. Proceedings of the 3rd International Conference. Elsevier Science Publishers, Barcelona, Spain.

Baldwin, B., Lomax, H., 1978. Thin layer approximation and algebraic model for separated turbulent flows. AIAA 78-0257.

Bendor, G., Igra, O., Wang, L., 2001. Shock wave reflections in dust-gas suspensions. J. Fluids Eng. 123, 145–153.

Carlson, D.J., Hoglund, R.F., 1964. Particle drag and heat transfer in rocket nozzles. AIAA J. 2, 1980–1984.

Carrier, G.F., 1958. Shock waves in a dusty gas. J. Fluid Mech. 4, 376–382.

Chang, I.S., 1980. One- and two-phase nozzle flows. AIAA J. 18, 1455–1461.

Choo, Y.K. (Ed.), 1995. Surface modeling, grid generation, and related issues in computational fluid dynamic (CFD) solutions, NASA-CP-3291. In: Proceedings of a Workshop held at NASA Lewis, Cleveland, Ohio.

Crowe, C.T., 1982. Review – numerical models for dilute gas–particle flows. J. Fluids Eng. 104, 297–303.

Dannenho_er, J.F., 1994. Multiblock grid generation. VKI Lecture Series 1994-02: Grid Generation.

Degani, David., Schiff, Lewis B., 1983. Computation of supersonic viscous flows around pointed bodies at large incidence. AIAA-83-0034.

Gilbert, M., Davis, D., Altman, D., 1955. Velocity lag of particles linearly accelerated combustion gases. Jet Propul. 25, 26.

Gokhale, S.S., Bose, T.K., 1989. Reacting solid particles in one-dimensional nozzle flow. Int. J. Multiphase Flow 15, 269–278.

Henderson, C.B., 1976. Drag coefficients of spheres in continuum and rarefied flows. AIAA J. 14, 707–708.

Hoglund, RF., 1962. Recent advance in gas–particle nozzle flows. ARS J. 32, 662–671.

Hunter, C.A., 1998. Experimental, theoretical, and computational investigation of separated nozzle flows. AIAA-98-3107.

Hwang, C.J., Chang, G.C., 1988. Numerical study of gas–particle flow in a solid rocket nozzle. AIAA J. 26, 682–689.

Igra, O., Elperin, I., Ben-Dor, G., 1999. Dusty gas flow in a converging–diverging nozzle. J. Fluids Eng. 121, 908–913.

Kliegel, J.R., 1959. One dimensional flow of a gas particle system. Space Technology Labs. TR-59-0000-00746.

Luo, X., Wang, G., Olivier, H., 2008. Parametric investigation of particle acceleration in high enthalpy conical nozzle flows for coating applications. Shock Waves 17, 351–362.

Lype, E.F., 1961. One dimensional analysis of non-isentropic two-phase flow. ARS Preprint 1605-61 (February).

Marconi, F., Rudman, S., Calia, V., 1981. Numerical study of one-dimensional unsteady particle-laden flows with shocks. AIAA J. 19, 1294–1301.

Mehta, R.C., Jayachandran, T., 1998. Fast algorithm to solve viscous two-phase flow in an axisymmetric rocket nozzle. Int J Numer Methods Fluids 26, 501–517.

Michael, L.N., Karl-Heinz, A.W., 1985. Supersonic Jets. Los Alamos Science (Spring/Summer).

Moshfegh, A., Ebrahimi, R., Shams, M., 1081. Simulation of truncated ideal contour nozzle separation considering external stream interactions. In: Proc. ImechE, Part G. J Aerospace Eng. 222, 1081–1095. doi:10.1243/09544100JAERO279.

Nishida, M., Ishimaru, S., 1990. Numerical analysis of gas–solid two-phase nonequilibrium nozzle flows. JSME Int. J. Ser. 33, 494–500.

Ounis, H., Ahmadi, G., 1990. Analysis of dispersion of small spherical particles in a random velocity field. J. Fluids Eng. 112, 114–120.

Roe, P.L., 1986. Characteristics based schemes for the Euler equations. A Numer Rev Fluid Mech, 337–365.

Shuen, J.S., Yoon, S., 1988. Numerical study of chemically reacting flows using an LU scheme. AIAA 0436.
Smith, R.E. (Ed.), 1992. Software systems for surface modeling and grid generation, NASA CP 3143. In: Proceedings of a Workshop held at NASA Langley, Hampton, VA.
Tsai Y.L.P., Hsieh K.C., 1990. Comparative study of computational efficiency of two LU schemes for non-equilibrium reacting flows. AIAA 90-0396.
Van Leer, B., 1982. Flux-vector splitting for the Euler equations. ICASE Report 82-30.
Vatsa, V.N., Sanetrik, M.D., Parlette, E.B., 1995. Block-structured grids for complex aerodynamic configurations: current status. In: Proceedings Surface Modeling, Grid Generation, and Related Issues in Computational Fluid Dynamic (CFD) Solutions, NASA-CP-3291.
Warren, M.R., Hartnett, J.P., Cho, Y.I., 1988. Hand Books of Heat Transfer. 3rd ed.. MC-Graw Hill.
Weast, R.C., Astle, M.J., Beyer, W.H., 1985. Handbook of Chemistry and Physics, 65th ed. CRC.
Weatherill, N.P. (Ed.), 1990. Numerical Grid Generation. VKI Lecture Series 1990-06.
Weatherill, N.P. (Ed.), 1994. Grid Generation. VKI Lecture Series 1994-02.
Weatherill, N.P., Eiseman, P.R., Hauser, J., Thompson, J.F. (Eds.), 1994. Numerical Grid Generation in Computational Fluid Dynamics and Related Fields. Proceedings of the 4th International Conference. Pineridge Press, Swansea, Wales.
White, F.M., 2006. Viscous Fluid Flow. Mc-Graw Hill, New York. p. 441.